Microstructural details of hydrogen diffusion and storage in Ti–V–Cr alloys activated through surface and bulk severe plastic deformation

Marc Novelli, Kaveh Edalati, Shota Itano, Hai-Wen Li, Etsuo Akiba, Zenji Horita, Thierry Grosdidier

Microstructural Details of Hydrogen Diffusion and Storage in Ti-V-Cr Alloys Activated Through Surface and Bulk Severe Plastic Deformation

Marc Novelli[1,2,*], Kaveh Edalati[3,4], Shota Itano[3], Hai-Wen Li[3,5,6], Etsuo Akiba[3,5], Zenji Horita[3,4], Thierry Grosdidier[1,2]

[1] Université de Lorraine, Laboratory of Excellence on Design of Alloy Metals for low-mass Structures (DAMAS), Metz F-57045, France

[2] Université de Lorraine, Laboratoire d'Etude des Microstructures et de Mécanique des Matériaux (LEM3 UMR 7239), 7 rue Félix Savart, BP 15082, Metz F-57073, France

[3] WPI, International Institute for Carbon-Neutral Energy Research (WPI-I2CNER), Kyushu University, Fukuoka, Japan

[4] Department of Materials Science and Engineering, Faculty of Engineering, Kyushu University, Fukuoka, Japan

[5] International Research Center for Hydrogen Energy, Kyushu University, Fukuoka, Japan

[6] Kyusyu University Platform of Inter/Transdisciplinary Energy Research, Fukuoka, Japan

Abstract

Structural observations were carried out on particles obtained after hydrogenation cycling of the $Ti_{25}V_{50}Cr_{25}$ and $Ti_{10}V_{75}Cr_{15}$ alloys processed by surface or bulk severe plastic deformation using the surface mechanical attrition treatment (SMAT) and high-pressure torsion (HPT) techniques, respectively. The produced particles differ in morphologies and fracture mode due to the differences in hydrogen diffusion paths. The fracture mode for the SMAT-processed samples with the gradient microstructure was mainly intragranular, whereas it was intergranular for the nanograined HPT processed samples. Hydrogen diffusion, which initiated at the grain boundaries on the surface, created Ti-rich and V-lean areas. The powders contained mainly β-VH monohydride and partly γ-VH_2 dihydride, and an orientation relationship of $(100)_\beta$ // $(110)_\gamma$ and $[001]_\beta$ // $[001]_\gamma$ with an angular deviation of ~2.5° was observed between the two phases using the electron backscattered diffraction (EBSD) analysis.

Keywords: Hydrogen storage, Vanadium-Based Alloy, Surface Mechanical Attrition Treatment (SMAT), High Pressure Torsion (HPT), Structural Defects, Hydrogen-induced Pulverization

Corresponding author
*marc.novelli@univ-lorraine.fr | Université de Lorraine, Laboratoire d'Etude des Microstructures et de Mécanique des Matériaux (LEM3 UMR 7239), 7 rue Félix Savart, BP 15082, Metz F-57073, France | +33 3 72 74 78 27

1. Introduction

The use of hydrogen as a fuel (associated with oxygen) represents a promising and sustainable approach for energy production. However, its use remains challenging considering its needs to be stored safely and compactly at room temperature. Nowadays, hydrogen is employed rather as a gas, requiring special tanks under high pressure, or as liquid needing a very low temperature storage (-252 °C), which is incompatible with an everyday use design [1].

Another possible approach consists of storing hydrogen in solid matrices using reversible reactions between solid metals and hydrogen through the formation of metal hydrides [2,3]. Several materials like Mg-based [4,5] or TiFe [6,7] alloys have demonstrated the feasibility of such an approach. Among these materials stand also the Ti-V-based alloys [8–11] which present the advantages to have a high volumetric storage capacity [12,13] associated with the ability to absorb and desorb the hydrogen at room temperature [12,14]. However, these alloys suffer from two main drawbacks: i) they require an initial high-temperature thermal activation and ii) they present slow diffusion kinetics.

Different methods have been proposed to overcome these kinetic drawbacks like matrix doping [15,16], alloying substitution [17,18] or microstructural lattice defect creation [19,20]. The latter method involves the use of structural defects (grain boundaries, dislocations, vacancies …) as short circuits for the hydrogen diffusion. In a recent work, the current authors [21] compared the effect of severe plastic deformation (SPD) carried out on i) bulk sample by high-pressure torsion (HPT) method [22,23] and ii) the surface by surface mechanical attrition treatment (SMAT) method [24,25] on the hydrogen storage kinetics of $Ti_{10}V_{75}Cr_{15}$ and $Ti_{25}V_{50}Cr_{25}$ alloys. The results showed that both processing routes led to the activation of the matrix at room temperature with a hydrogen absorption up to ~4 wt%. However, the bulk nanostructured samples heavily deformed by HPT, which easily stored

hydrogen, did not show any desorption. Comparatively, the materials processed by SMAT and having a gradient microstructure could reversibly absorb and desorb hydrogen. This apparently surprising behaviour was rather consistent with the results of Couillaud et al. [26] who have showed that the lattice defects can hinder the hydrogen desorption of a $TiV_{1.6}Mn_{0.4}$ alloy severely deformed by ball milling.

The reason for these opposite trends between the two types of materials processed by HPT and SMAT was not clear and, in general, there is a wide lack of understanding on the contributions of different structural defects on the i) hydrogen absorption/diffusion, and ii) hydrogen trapping/releasing. Therefore, the aim of the present contribution is to carry out post-mortem observations of the SMAT- and HPT-processed materials, after their hydrogenation, in order to gain some new insights on the effect of different structural defects on the hydrogen storage behaviours.

2. Material and experimental techniques

Two vanadium-based alloys were used in this study: $Ti_{10}V_{75}Cr_{15}$ and $Ti_{25}V_{50}Cr_{25}$. They were prepared by arc melting under an argon inert atmosphere within a water-cooled copper mold leading to a microstructure with a grain size in the range of 50-500 µm. No additional heat treatment was applied on the elaborated ingots. Then, 10 mm diameter discs were cut by electric discharge and mechanically polished to a thickness of 0.8 mm.

The microstructures were modified, in very different ways, by two different SPD processing techniques. For the first type of modification, gradient microstructures were produced by the SMAT process using 2 mm diameter AISI 52100 steel medias to shot-peened the surface. The sample surfaces were treated during 480 s with a vibrating amplitude of 60 µm and a frequency of 20 kHz using a Stressonic device developed by Sonats [27]. For the

second modification, the bulk-nanograined samples were produced by HPT process using a hydrostatic pressure of 6 GPa and 100 turns (rotation speed: 1 rpm) at room temperature.

These two processing techniques lead to different microstructures which are recalled in Figure 1 (additional details can be found in [21]). TEM images were selected to describe the HPT-processed sample due to its very fine nanostructure. The surface deformation induced by the SMAT leads to the creation of a nanostructure along the first microns of the extreme surface associated to a strain gradient towards the sample core [28] (Figure 1a). In addition (as will be discussed afterwards), numerous cracks were generated due to the brittleness of the V-based samples (see close-view). In comparison, the HPT bulk process generates a nanostructure (Figure 1b) having grain sizes of 30-40 nm in the whole sample that was free from any cracks (see close-view), thanks to the applied hydrostatic pressure during shear deformation.

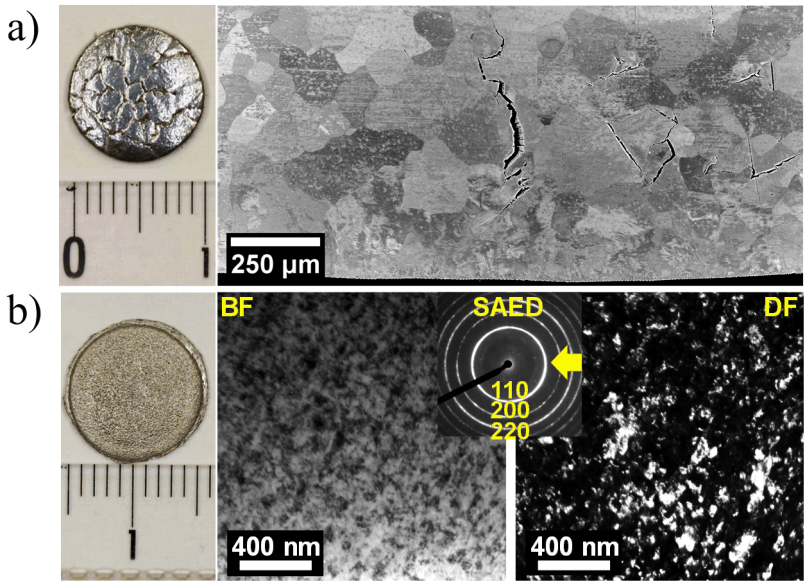

Figure 1 $Ti_{10}V_{75}Cr_{15}$ macroscopic views and associated microstructures before hydrogenation for a) the SMAT- (SEM) and b) HPT-processed (TEM) samples.

The materials after processing by SMAT and HPT were hydrogenated and dehydrogenated for two cycles at 303 K and one cycle at 353 K to achieve pressure-composition-temperature (PCT) isotherms, as described in details in an earlier paper [21]. The

materials after the third hydrogen storage cycle were in the form of pulverized particles. Indeed, because of the hydrogen storage cycles, the initially large samples fracture into powder particles. In order to make the reading more convenient, the particles produced by the repeated hydrogenation of the SMAT- and HPT-processed samples will be called in the following text "SMAT particles" and "HPT particles", respectively.

The characterization of morphological aspect of the cycled particles as well as their inner structure viewed on polished surfaces were both done on a Zeiss Supra 40 scanning electron microscope (SEM). A secondary electron (SE) contrast and a back-scattered electron (BSE) contrast were used for the morphological and cross-section observations, respectively. Energy dispersive spectroscopy (EDX) quantifications were carried under a tension of 20 kV (10^6 counts were required to stop the measurements). The electron backscattered diffraction (EBSD) acquisition was done using a tension of 20 kV (12 bands were required for pattern indexation) ands then post-treated using the ATEX (Analysis Tools for Electron and X-ray Diffraction) software [29].

3. Results

3.1 Particle size and morphology

Table 1 gives the major features revealed for the two alloys and different processing techniques (HPT and SMAT) in terms of particle sizes and morphological aspects.

Table 1 Average particles sizes of hydrogenated $Ti_{10}V_{75}Cr_{15}$ and $Ti_{25}V_{50}Cr_{25}$ alloys after processing by SMAT and HPT.

	SMAT	HPT
$Ti_{10}V_{75}Cr_{15}$	Bimodal 10 µm + 130 µm Sharp edges	900 µm Smooth edges
$Ti_{25}V_{50}Cr_{25}$	Bimodal 10 µm + 325 µm Sharp edges	410 µm Smooth edges

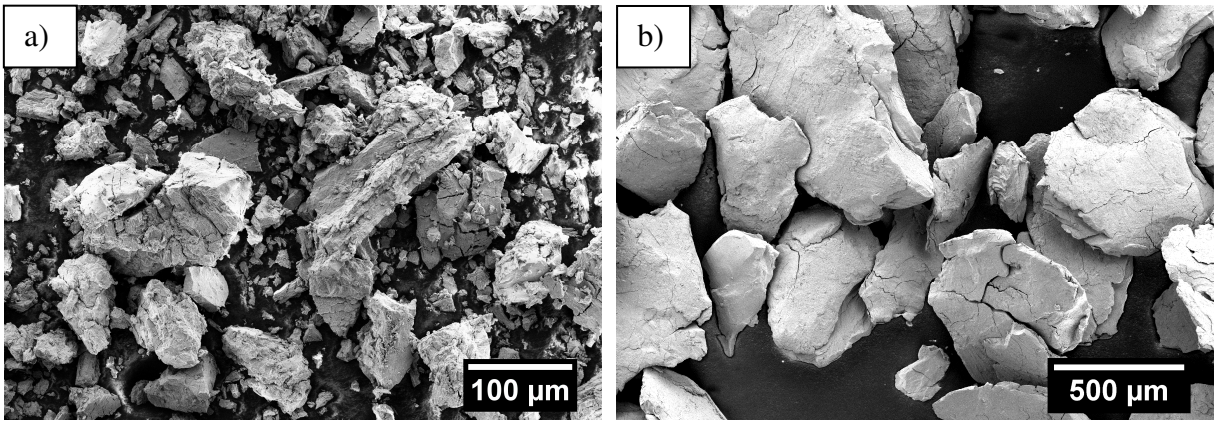

Figure 2 SE contrast SEM observations of the hydrogenated $Ti_{10}V_{75}Cr_{15}$ alloy after processing by a) SMAT and b) HPT.

As an example, the particles obtained after hydrogenation of the $Ti_{10}V_{75}Cr_{15}$ alloy are presented in Figures 2a and b for the SMAT and HPT particles, respectively. Two populations of particles are visible for the SMAT particles, one with very small sizes of about 10 µm and another one with much larger sizes (Figure 2a). These large SMAT particles have a mean size of 130 µm and possess sharp edges. Comparatively, the HPT particles (Figure 2b) are much bigger in size with a mean value of about 900 µm. Additionally, their shapes are smooth with less fragments than the ones obtained on the SMAT particles (Figure 2a).

Concerning the particles coming from the hydrogenation of the $Ti_{25}V_{50}Cr_{25}$ alloy, the trend is the same as the $Ti_{10}V_{75}Cr_{15}$ alloy: finer particles are generated after hydrogenation of the SMAT-processed sample having also a bimodal distribution. However, the difference in particles size is less pronounced compared with the $Ti_{10}V_{75}Cr_{15}$ alloy: mean sizes of 325 µm and 410 µm were measured for the SMAT and HPT particles, respectively.

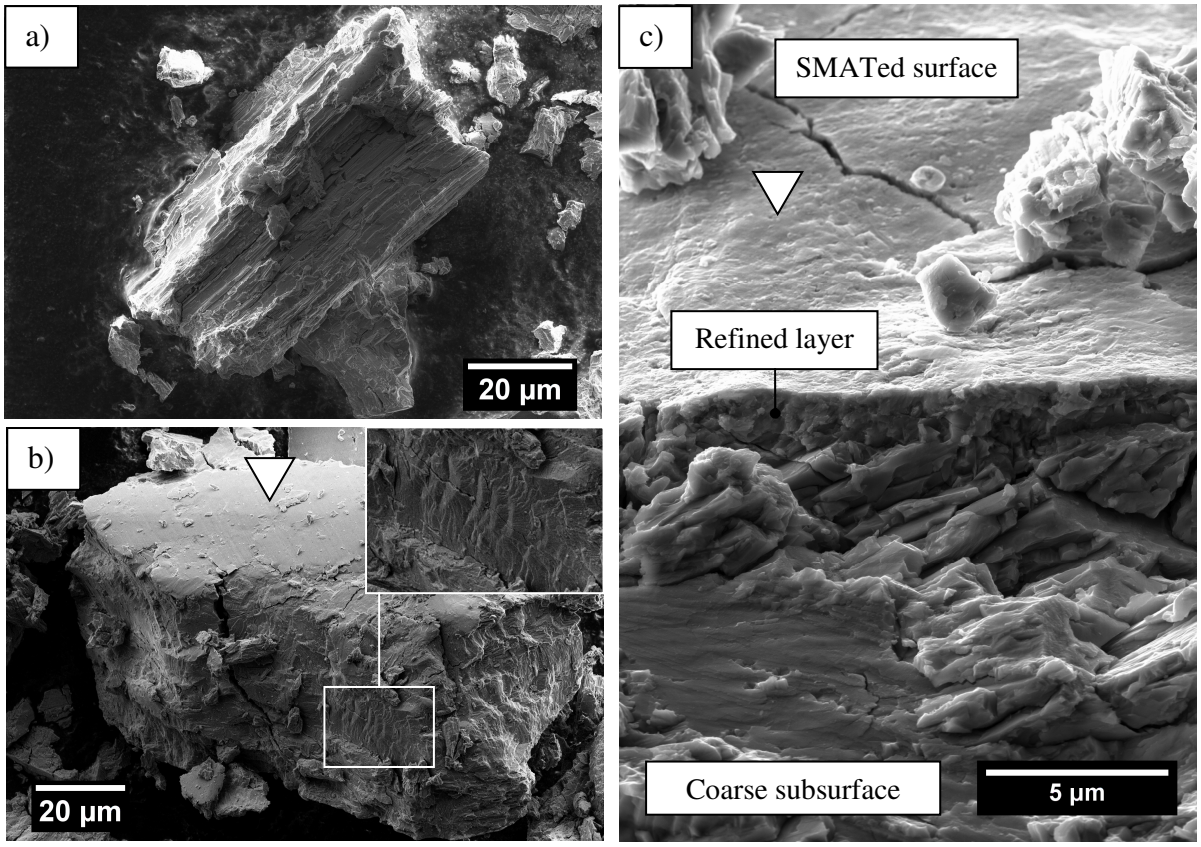

Figure 3 SE contrast SEM observations of the particles obtained on the hydrogenated $Ti_{10}V_{75}Cr_{15}$ after processing by SMAT.

Close-views of the particles coming from hydrogenation of SMAT- and HPT-processed $Ti_{10}V_{75}Cr_{15}$ alloy can be seen in Figures 3 and 4, respectively. Large flat surfaces, that are the external surfaces of the initial disc samples, are marked by white triangles in Figures 3 and 4. The particle in Figure 3a possesses sharp facets which were associated with a brittle fracture. The other particle in Figure 3b also possessed brittle fracture surfaces below the initial surface that is marked with a white triangle in Figure 3b. The close view in the inset of Figure 3b shows a crack path characterized by a crack parallel to the initial surface which has generated several semi-hemispherical stress-concentration sites. This indicates that the crack did not propagate continuously but, instead, was stopped several times during its propagation.

Figure 3c shows a higher magnification SEM image taken directly at the surface that was previously peened by the SMAT process. This surface, on the upper side and marked

with a triangle, could be recognized easily by its undulated aspect generated by the shot impacts. The refined layer generated by the SMAT is clearly visible along the first few microns under the treated surface and is followed by a coarser structure. It is interesting to note that this gradient structure is not as pronounced as the gradient structure generally observed after SMAT of ductile materials such as Al [30], Cu [31,32] or austenitic stainless steel [33–36]. This is because of the brittle nature of the Ti-V-Cr alloys.

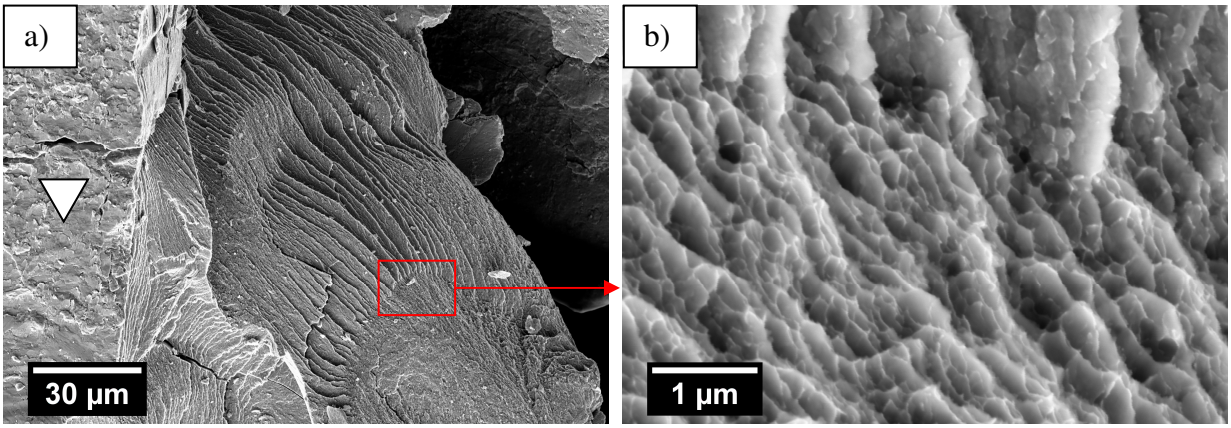

Figure 4 SE contrast SEM observations of the particles obtained on the HPT-processed $Ti_{10}V_{75}Cr_{15}$ sample.

Detailed views of an HPT particle are presented in Figure 4 for the $Ti_{10}V_{75}Cr_{15}$ alloy. The observed features differ significantly from the ones observed on the SMAT particles. The nanostructure generated by the HPT process before hydrogenation is clearly visible in the close-view in Figure 4b. The ultrafine grains produced under the HPT processing are surrounded by a different type of contrast along the grain boundaries. As grain boundaries are known to be shortcuts for diffusion, it is likely that this contrast witnesses hydrogen diffusion along the grain boundaries where the "brittle" fracture subsequently took place.

As seen in the upper part of the image in Figure 4a, a particular structure containing numerous elongated features is visible. It suggests a hydrogen-induced cleavage propagation along the shear direction previously generated during the HPT processing. These structures are indeed thought to be induced by the hydrogen paths created during hydrogen diffusion that are, possibly, driven by some local strain heterogeneities [37].

3.2 Phase analysis and internal structure

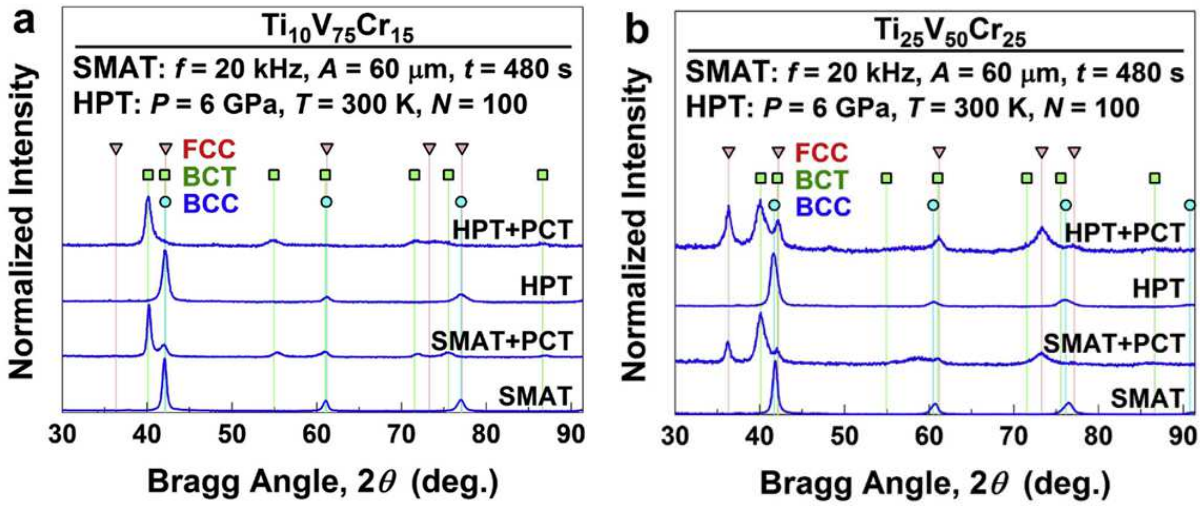

Figure 5 XRD acquisitions carried out before and after three PCT cycles for a) the $Ti_{10}V_{75}Cr_{15}$ and b) the $Ti_{25}V_{50}Cr_{25}$ alloys processed by SMAT and HPT [21].

Figure 5 presents the XRD diffraction patterns obtained before and after hydrogenation/dehydrogenation cycling of the $Ti_{10}V_{75}Cr_{15}$ (Figure 5a) and $Ti_{25}V_{50}Cr_{25}$ (Figure 5b) alloys for both the SMAT- and HPT-processed samples. Initially, both alloys were characterized by a fully body-centred cubic (BCC) structure and no phase transformation was detected by XRD neither for the SMAT- nor the HPT-processed samples despite the severity of the deformation. As a reminder, the hydrogen absorption presents two steps in the V-based alloys: i) the creation of a stable VH monohydride with the body-centred tetragonal (BCT) structure at low-pressure levels (~0.1 Pa) followed by the formation of a less-stable VH_2 dihydride with the face-centred cubic (FCC) structure at higher pressures (~0.1 MPa).

After hydrogenation of the $Ti_{10}V_{75}Cr_{15}$ alloy, only the β-VH (BCT) phase was mainly detected in the SMAT and HPT particles, but small amounts of BCC and FCC phases are also present (Figure 5a). Taking into account the PCT behaviours published previously [21] and keeping in mind that two types of deformation processes were used, this analysis outlines 2 different phenomena. For the SMAT-processed sample, the β-VH (BCT) hydride absorbs the

hydrogen to form the γ-VH_2 (FCC) which, thereafter, desorbs the hydrogen. The β-VH (BCT) hydride remains active during further cycling for β-VH (BCT) to γ-VH_2 (FCC) transition. However, for the HPT-processed sample, despite initial activation, the β-VH (BCT) hydride is deactivated in the following cycles and cannot further store the hydrogen. As discussed in this manuscript, the reason for deactivation of β-VH (BCT) phase in HPT-processed sample is due to the presence of large fraction of lattice defects and grain boundaries which hinder the hydrogen reversion.

Comparatively, both the BCT and FCC hydrides were indexed for the $Ti_{25}V_{50}Cr_{25}$ samples in Figure 5b. Thus, the γ-VH_2 (FCC) → β-VH (BCT) was not completely induced in this alloy to desorb the hydrogen. However, the FCC hydride (111) peak is more intense for the HPT particles than the one measured on the SMAT particles which indicates a higher proportion of remaining γ-VH_2 hydrides in the HPT particles.

The presence of three BCC, BCT and FCC phases in Figure 5, especially for the $Ti_{25}V_{50}Cr_{25}$ alloy, is probably due to the kinetics of hydrogen absorption and desorption. Indeed, since the $Ti_{25}V_{50}Cr_{25}$ alloy has a lower plateau pressure than the $Ti_{10}V_{75}Cr_{15}$ alloy, the co-existence of three phases in this alloy is more significant as there is less driving force for dehydrogenation in this alloy.

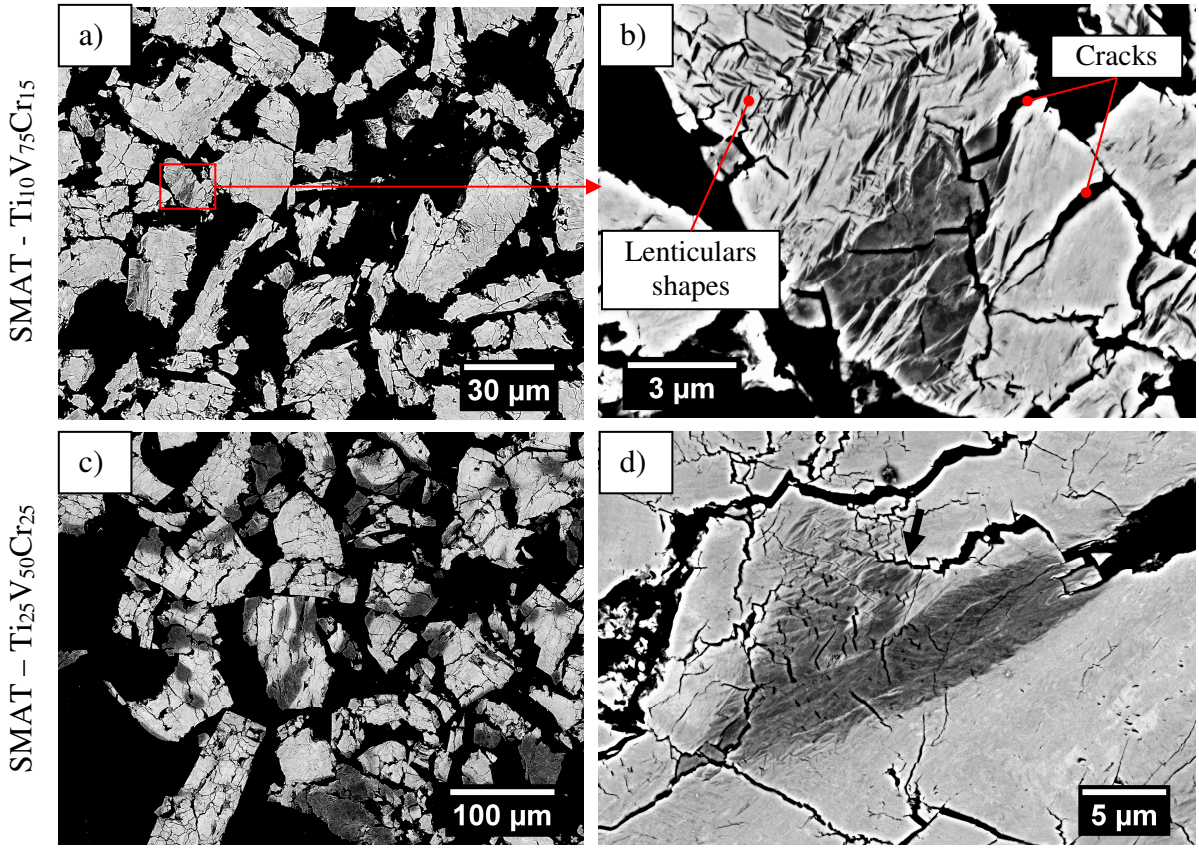

Figure 6 BSE contrast SEM observations of the cross section of SMAT-processed (a-b) $Ti_{10}V_{75}Cr_{15}$ and (c-d) $Ti_{25}V_{50}Cr_{25}$ alloys after hydrogenation.

In order to gain more insights in the inner structures of the cycled particles, SEM observations were carried out on polished cross-sections (Figure 6 and 7). Figure 6a and c shows a general view of the SMAT particles coming from the $Ti_{10}V_{75}Cr_{15}$ and $Ti_{25}V_{50}Cr_{25}$ alloys, respectively. Numerous inner cracks that fragmented the particles can be seen in both alloys. In addition, a very sharp grey contrast can be depicted especially in the $Ti_{25}V_{50}Cr_{25}$ sample (Figure 6c). This contrast consists, for both alloys, in an intricated lenticular aspect, as it can be better seen in the $Ti_{10}V_{75}Cr_{15}$ sample (Figure 6b). Additionally, a particular crack propagation pathway can be seen in Figure 6d, as indicated by a black arrow. This pathway describes a step-by-step crack propagation reflecting that the crack stopped and re-propagated several times during the hydrogenation cycling process.

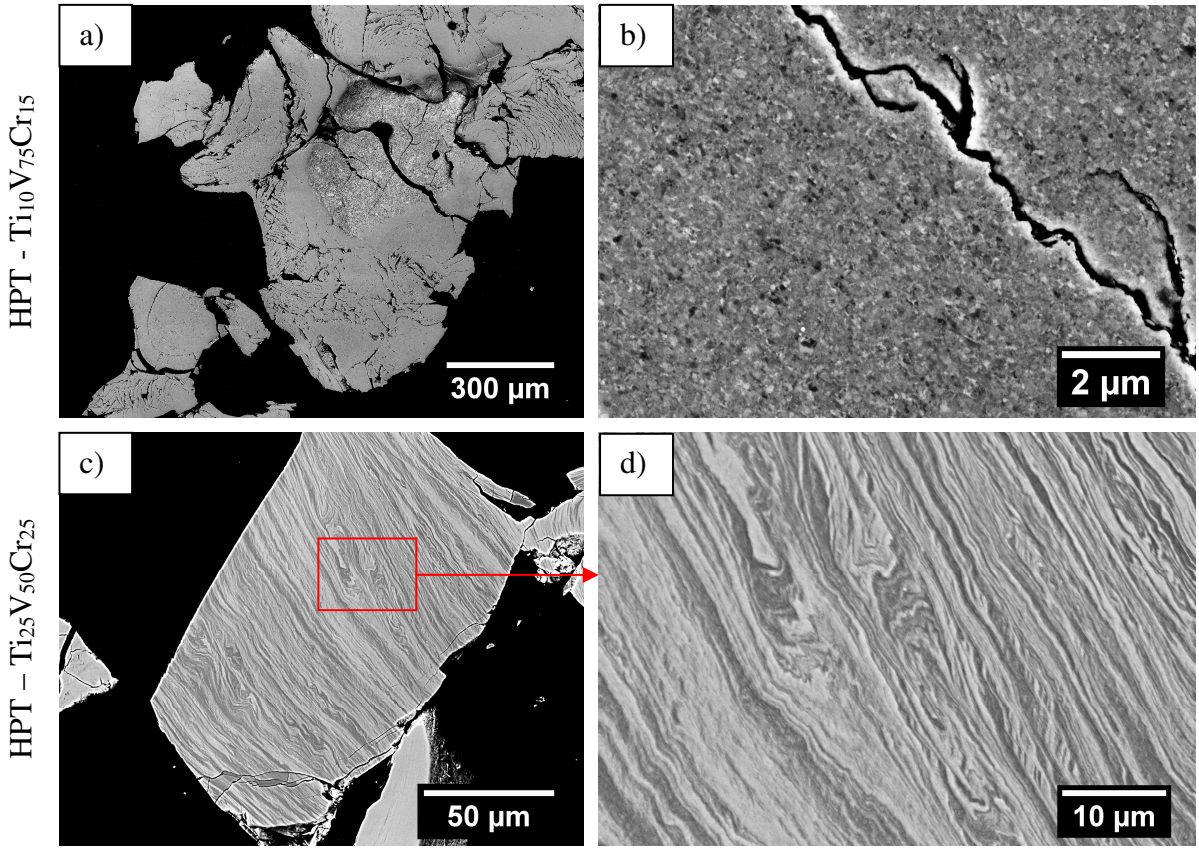

Figure 7 BSE contrast SEM observations of the cross section of HPT-processed (a-b) $Ti_{10}V_{75}Cr_{15}$ and (c-d) $Ti_{25}V_{50}Cr_{25}$ alloys after hydrogenation.

Figure 7 shows the inner structures of HPT particles coming from hydrogenation of $Ti_{10}V_{75}Cr_{15}$ (Figures 7a and b) and $Ti_{25}V_{50}Cr_{25}$ (Figures 7c and d) alloys. The density of inner cracks was much lower than that of the SMAT particles. No sharp contrast was observed on the $Ti_{10}V_{75}Cr_{15}$ sample (Figure 7a) and only the crystallographic orientation coming from the nanostructure generated by the HPT treatment was visible all over the particle cross-sections (Figure 7b). The absence of bright/dark zones is likely due to the fact that this alloy was essentially single phase after the hydrogen storage process (HPT+PCT in Figure 5a). However, the HPT-processed $Ti_{25}V_{50}Cr_{25}$ alloy presented a substantial chemical contrast after hydrogenation (Figure 7c) characterized by elongated domains. Here, the elongated contrast describes a band-like structure, probably an aspect inherited from the shear strain and/or

hydrogenation. Contrary to the SMAT particles, no lenticular features were observed on the HPT particles.

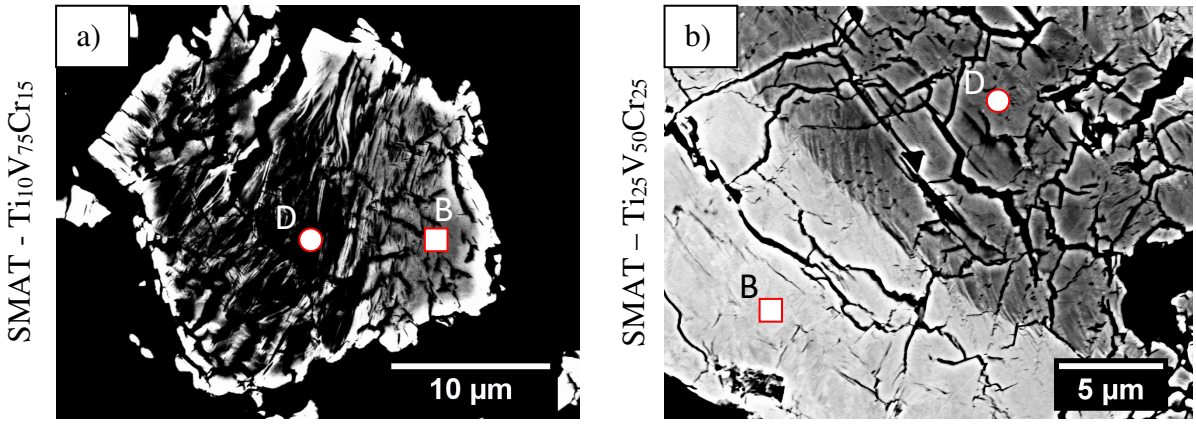

Figure 8 BSE contrast SEM observations of the a) $Ti_{10}V_{75}Cr_{15}$ and b) $Ti_{25}V_{50}Cr_{25}$ alloys after processing by SMAT and hydrogenation. EDX quantifications are given in Table 2.

Table 2 EDX quantifications carried out on the bright and dark zones of $Ti_{10}V_{75}Cr_{15}$ and $Ti_{25}V_{50}Cr_{25}$ alloys in Figure 7 after processing by SMAT and hydrogenation.

		Ti [at%]	**V** [at%]	**Cr** [at%]
$Ti_{10}V_{75}Cr_{15}$	**Bright Zone**	10.2	75.7	14.1
	Dark Zone	15.6	69.9	14.5
$Ti_{25}V_{50}Cr_{25}$	**Bright Zone**	25.4	50.3	24.3
	Dark Zone	35.9	42.0	22.1

EDX chemical analyses were carried out on two SMAT particles of the $Ti_{10}V_{75}Cr_{15}$ (Figure 8a) and $Ti_{25}V_{50}Cr_{25}$ (Figure 8b) alloys. The rounded and squared shapes in the images represent the locations of the chemical acquisitions done on the dark and bright contrasted zones, respectively. The related EDX quantifications are given in Table 2. For both alloys, the bright zones – which were essentially featureless and did not contain lamellar structures - correspond fairly well to the initial alloy compositions. Comparatively, the dark zones – which were more heavily cracked and often presented the lenticular contrast - presented a higher fraction of titanium associated with a lower fraction of vanadium and a rather stable

fraction of chromium. Thus, because of these structural aspects, the Ti-rich and V-lean zones must correspond to the zones that remained hydrided.

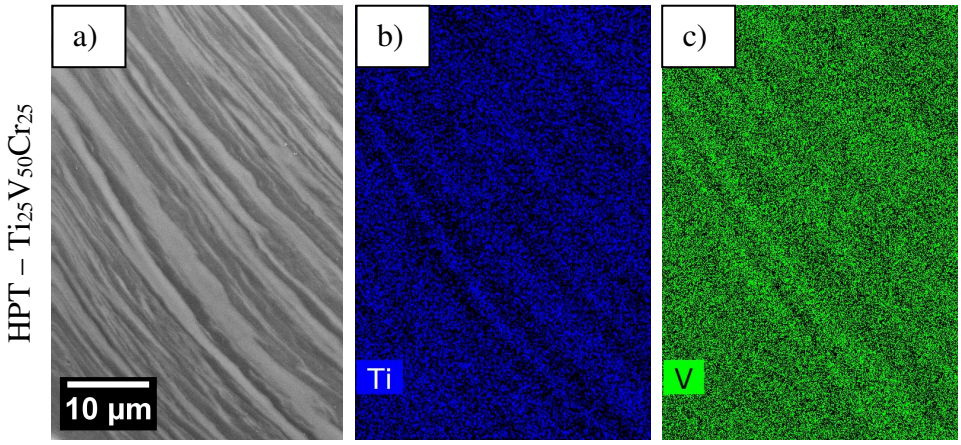

Figure 9 (a) SE contrast SEM observations and associated EDX mapping with b) Ti and c) V carried out on the $Ti_{25}V_{50}Cr_{25}$ alloy after processing by HPT and hydrogenation.

Figure 9 shows another EDX acquisition carried out on a $Ti_{25}V_{50}Cr_{25}$ HPT particle. The successive elongated bright and dark zones which are visible in Figure 9a are also characterized by chemical composition differences, as observed previously on a SMAT particle in Figure 8. Regarding the alloying element maps (Figure 9b and c), the bands alternate successively with elongated Ti-rich (dark zones) and V-rich (bright contrast) zones.

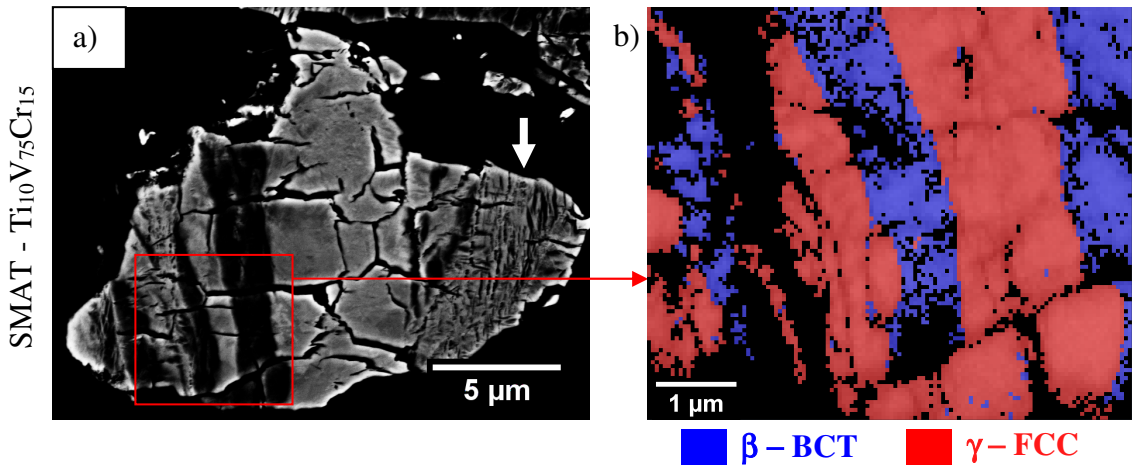

Figure 10 a) BSE contrast acquisition and b) EBSD phase map for the $Ti_{10}V_{75}Cr_{15}$ alloy after processing by SMAT and hydrogenation (β-BCT in blue, γ-FCC in red)

Further details were obtained by EBSD on the sharp contrast seen in the $Ti_{10}V_{75}Cr_{15}$ SMAT particle (Figure 10). Even though these particles gather several features impeding the indexation of EBSP (numerous cracks, high stresses …), the lattice structures of the different zones were acquired without any problem and where best indexed as the β-BCT and γ-FCC structures. From these results, it is clear that the changes in chemistry in Figure 8 and Table 2 are related to the phase changes. The bright zones correspond to the BCT hydride whereas the dark zones correspond to the FCC hydride. Detailed analysis of the EBSD data has also revealed that the orientation relationship given by Wanagel et al. [38] as $(100)_\beta$ // $(110)_\gamma$ and $[001]_\beta$ // $[001]_\gamma$ is followed here with a mean deviation of ~2.5°. This angular deviation is likely due to hydrogen diffusion and metastability of the FCC hydride. An EBSD acquisition was also carried out on the lenticular structures present on the right side of the particle in Figure 10 (white arrow) but no indexation was possible because of their small sizes and highly blurred Kikuchi's patterns that witnessed highly strained areas.

4. Discussion

The purpose of this study was to document the mechanisms taking place during the hydrogenation cycling of initial bulk samples with gradient microstructure and nanostructure processed by a surface (SMAT) or a bulk (HPT) SPD processes. The following discussion will be divided into two sections dealing with (i) the general aspects of the particles formed by the hydrogen-induced pulverization and (ii) the inner structure to get details on the hydrogen diffusion mechanisms.

4.1 Particle sizes and aspects generated after hydrogenation

Repeated hydrogenation of metallic samples led to fragmentation of the initially bulk samples toward powder particles. This fragmentation mechanism is known as hydrogen pulverization [39,40] which is governed by the repeated expansion/contraction of the lattice volume induced by the hydrogen diffusion. Such a process is usually considered beneficial in solid-state hydrogen storage studies because the fragmentation process increases the overall interaction surface area and leads to fresh, non-oxidized new surfaces [41].

It was shown that the different Ti-V-Cr alloys and processing methods led to different particle sizes (Table 1). Despite an initial coarse microstructure (Figure 1a), the SMAT-processed samples generated a bimodal particle size with fine particles of about 10 µm and larger particles of about 130 µm and 325 µm for the $Ti_{10}V_{75}Cr_{15}$ alloy and the $Ti_{25}V_{50}Cr_{25}$ alloys (Figure 2), respectively. Comparatively, the initial nanostructure (Figure 2a) of the HPT-processed samples led to particle sizes of about 900 and 410 µm after exactly the same number of hydrogenation cycles for the $Ti_{10}V_{75}Cr_{15}$ and the $Ti_{25}V_{50}Cr_{25}$ alloys (Figure 2b), respectively. As the HPT-processed samples were able to absorb hydrogen efficiently but unable to desorb it completely, this has led to coarser particles than those for the SMAT-processed samples. Indeed, the SMAT-processed samples absorbed the hydrogen and desorbed it for three cycles, leading to finer particles.

The particles coming from the two deformation treatments also showed completely different morphologies. The SMAT particles possessed sharp edges with parallel lines whereas the HPT particles possessed smooth faces with elongated cleavage structures parallel to the shear strain direction taking place during HPT. Along these root-like structures, the HPT particles exhibit smooth faces and a clear nanostructure as seen in Figure 4. This kind of fracture faces was also observed by Hohenwarter et al. [42] on a pure vanadium sample processed by HPT and interpreted as a micro-ductile fracture, leaving each nanograins visible. The question whether the fracture is micro-ductile or has a brittle character is beyond the

scope of the present paper. However, it is clear that the hydrogen path was along the grain boundaries in the HPT particles. Since the fracture in the HPT-processed samples occurring at the boundaries of the ultrafine rounded and equiaxed grains, the surface aspects of the HPT particles are overall rather smooth.

While it is clear that the pathway for hydrogen diffusion was along the grain boundaries for the HPT-processed samples, it was essentially intragranular within the coarse-grained core of the SMAT-processed samples. Indeed, as a mechanical surface treatment, the SMAT generates a structural refinement at the treated extreme surface with a lot of grain boundaries and plastic defects (Figure 1) promoting the hydrogen diffusion in the early stage of the hydrogenation process. Then, the hydrogen moves towards the coarse grain subsurface where the diffusion becomes essentially intragranular. This leads to the formation of straight brittle fracture surface (Figure 3a). As proposed by Torres et al. [43] who studied the diffusion of hydrogen in vanadium, this involves the formation of barrier which impedes the movement of dislocations, leading to the formation of successive crack fronts, as it can be seen in the close-view of Figure 3b and the particular crack path observed in Figure 6d.

4.2 Particles inner structures

Concerning the inner microstructure of the particles, bright and dark zones associated to a two-phase mixture were observed in all powder particles except for the HPT-processed $Ti_{10}V_{75}Cr_{15}$ alloy that was single phased after the PCT experiments (Figure 5a). The EBSD acquisition map in Figure 10 for the $Ti_{10}V_{75}Cr_{15}$ SMAT particle revealed that the dark zones, which were also characterized by different chemistry than the rest of the sample, corresponded to the FCC VH_2-dihydrides.

The FCC dihydride phase was revealed more clearly in the XRD diffractograms of the $Ti_{25}V_{50}Cr_{25}$ alloy in addition to the BCT and small amount of initial BCC phase. The presence of larger amount of FCC phase in this alloy is due to the higher stability of FCC phase in the $Ti_{25}V_{50}Cr_{25}$ alloy compared with the $Ti_{10}V_{75}Cr_{15}$ alloy [21]. Additionally, a chemical composition variation was measured between the two types of zone (Figure 8 and Table 2) in which the dark zones of FCC VH_2-dihydrides were Ti-rich and V-poor compared with the rest of the material. It could have been considered that these zones were the result of chemical heterogeneities that could build up during the casting of the initial materials. However, these Ti-rich and V-lean alternate areas were also observed after hydrogenation of the $Ti_{25}V_{50}Cr_{25}$ HPT-processed alloy (Figure 7 and 9). As the HPT method is known to mix the alloying elements under very high strain (especially by using large number of turns as 100) - as observed for example on the Mg-based systems [44] - the presence of these heterogeneous zones in the $Ti_{25}V_{50}Cr_{25}$ alloy after HPT processing and hydrogenation (Figure 7d) indicates that the differences in chemistry are mainly related to the hydrogenation process. It is possible that they have built up during the hydrogen storage process to facilitate the hydrogen penetration.

For the SMAT-processed sample, hydrogen diffused first through the nanostructure and cracks generated on the treated surface. Then, the hydrogen diffused within the coarse-grained matrix to create large domains (Figure 6) of Ti-rich (V-lean) FCC hydrides (Figure 8), as revealed by EBSD analysis in Figure 10. The presence and fraction of bright/dark zones were reasonably consistent with the PCT measurements [21]. Indeed, the $Ti_{10}V_{75}Cr_{15}$ SMAT-processed sample only had few dark zones (Figure 6a) due to the ability of this product to desorb the hydrogen, leaving a small amount of FCC hydrides.

In the case of the HPT particles, the diffusion of hydrogen has been promoted along the shear direction imposed during the SPD processing. This is clearly seen in the $Ti_{25}V_{50}Cr_{25}$

HPT particles in which the fine contrast of alternate hydrided Ti-rich (V-lean) and non-hydrided domains is visible (Figure 9). When cracks propagate, this creates an elongated structure (Figure 4a) that also stretches along the microscopic shear direction of the HPT particles. This is believed to be related to local strain heterogeneities that can build-up during HPT processing and are known to affect the efficiency of the local hydrogen-activation process [45]. As the grain size in the HPT particles is extremely fine, the quantity of grain boundaries is such that they are the major option for hydrogen diffusion (Figure 4b). The reason why the elongated contrast along the microscopic shear plane is hardly visible for the $Ti_{10}V_{75}Cr_{15}$ HPT particles (Figure 7b) is due to the fact that this sample was essentially single phase after the hydrogenation process (Figure 5a). Thus, in the absence of chemical contrast, only the crystallographic contrast of grain orientations is visible. This is possibly due to the fact that the FCC hydride remained stable in the grain boundaries and its presence hinders the diffusion of hydrogen during cycling.

5. Conclusions

The powders generated after hydrogen pulverization of two Ti-V-Cr alloys processed by SMAT or HPT were investigated to gain new insights on the effect of hydrogen storage. Significant differences were observed in the size and aspect of the hydrogen-induced pulverized particles that, also, revealed the different hydrogen diffusion pathways for the materials activated by SMAT or HPT.

In both cases (SMAT and HPT particles), the preferential diffusion of the hydrogen atoms was assisted by segregations that led to variations in the chemical and internal hydride phase structure. An orientation relationship $(100)_\beta$ // $(110)_\gamma$ and $[001]_\beta$ // $[001]_\gamma$ has been observed between the BCT matrix and FCC hydride with an angular deviation of ~2.5°.

For the HPT heavily deformed and ultrafine-grained material, preferential diffusion of hydrogen atoms took place at the grain boundaries. Additionally, diffusion paths where also witnessed by an elongated structure associated with elongated chemical contrasts along the shear axis of the severely deformed products. These are likely due to shear heterogeneities generated during HPT and hydrogenation. In this case, the hydrogen pulverization process has led to the formation of fairly large (despite the nanostructured grains) particles that broke by a step-by-step crack propagation along the fine grain boundaries leading to fairly smooth particles.

For the SMAT-processed precursors, the ultrafine-grained structure at the surface of the shot peened samples derived the hydrogen atoms through the oxidized surface (by grain-boundary diffusion) before entering the coarse-grained core structure. Then, the hydrogen diffusion occurred essentially intragranularly in the coarse-grained core, opening and fracturing along transgranular cleavage planes that generate powder particles having sharp edges.

6. Acknowledgments

This study was supported in part by the MEXT, Japan, through a Grant-in-Aid for Scientific Research (S) (No. 16H04539 and 26220909), and in part by the French State through the program “Investment in the future” operated by the National Research Agency (ANR) and referenced by ANR-11- LABX-0008-01 (Labex DAMAS). The HPT process was carried out in the International Research Center on Giant Straining for Advanced Materials (IRC-GSAM), Kyushu University, Japan, and the ultrasonic SMAT process as well as the SEM microstructural characterizations were carried out within the IMPACT department in LEM3, University of Lorraine, France.

7. References

[1] Schlapbach L, Züttel A. Hydrogen-storage materials for mobile applications. Nature 2001;414:353–8.
[2] Sakintuna B, Lamari-Darkrim F, Hirscher M. Metal hydride materials for solid hydrogen storage: a review. Int J Hydrogen Energy 2007;32:1121–40.
[3] Rusman NAA, Dahari M. A review on the current progress of metal hydrides material for solid-state hydrogen storage applications. Int J Hydrogen Energy 2016;41:12108–26.
[4] Dornheim M, Doppiu S, Barkhordarian G, Boesenberg U, Klassen T, Gutfleisch O, et al. Hydrogen storage in magnesium-based hydrides and hydride composites 2007;56:841–6.
[5] Jain IP, Lal C, Jain A. Hydrogen storage in Mg : a most promising material. Int J Hydrogen Energy 2010;35:5133–44.
[6] Reilly JJ, Wiswall RH. Formation and properties of iron titanium hydride. Inorg Chem 1974;13:218–22.
[7] Schober T, Westlake DG, Division S. The activation of FeTi for hydrogen storage: a different view. Scr Metall 1981;15:913–8.
[8] Iba H, Akiba E. Hydrogen absorption and modulated structure in Ti–V–Mn alloys 1997;254:21–4.
[9] Cho S-W, Han C-S, Park C-N, Akiba E. The hydrogen storage characteristics of Ti–Cr–V alloys. J Alloys Compd 1999;288:294–8.
[10] Massicot B, Latroche M, Joubert J. Hydrogenation properties of Fe – Ti – V bcc alloys. J Alloys Compd 2011;509:372–9.
[11] Kumar S, Jain A, Ichikawa T, Kojima Y, Dey GK. Development of vanadium based hydrogen storage material: a review. Renew Sustain Energy Rev 2017;72:791–800.
[12] Akiba E, Iba H. Hydrogen absorption by Laves phase related BCC solid solution. Intermetallics 1998;6:461–70.
[13] Seo C, Kim J, Lee PS, Lee J. H ydrogen storage properties of vanadium-based b.c.c. solid solution metal hydrides 2003;348:252–7.
[14] Suwarno S, Solberg JK, Maehlen JP, Krogh B, Yartys VA. Influence of Cr on the hydrogen storage properties of Ti-rich Ti-V-Cr alloys. Int J Hydrogen Energy 2012;37:7624–8.
[15] Miraglia S, De Rango P, Rivoirard S, Fruchart D, Charbonnier J, Skryabina N. Hydrogen sorption properties of compounds based on BCC Ti1-xV1-yCr1+x+yalloys. J Alloys Compd 2012;536:1–6.
[16] Dixit V, Huot J. Structural, microstructural and hydrogenation characteristics of Ti-V-Cr alloy with Zr-Ni addition. J Alloys Compd 2019;776:614–9.
[17] Yukawa H, Takagi M, Teshima A, Morinaga M. Alloying effects on the stability of vanadium hydrides 2002;332:105–9.
[18] Towata S, Noritake T, Itoh A, Aoki M, Miwa K. Effect of partial niobium and iron substitution on short-term cycle durability of hydrogen storage Ti e Cr e V alloys. Int J Hydrogen Energy 2013;38:3024–9.
[19] Edalati K, Shao H, Emami H, Iwaoka H. Activation of titanium-vanadium alloy for hydrogen storage by introduction of nanograins and edge dislocations using high-pressure torsion. Int J Hydrogen Energy 2016;41:8917–24.
[20] Edalati K, Akiba E, Horita Z. High-pressure torsion for new hydrogen storage materials. Sci Technol Adv Mater 2018;19:185–93.
[21] Edalati K, Novelli M, Itano S, Li HW, Akiba E, Horita Z, et al. Effect of gradient-structure versus uniform nanostructure on hydrogen storage of Ti-V-Cr alloys: investigation using ultrasonic SMAT and HPT processes. J Alloys Compd

2018;737:337–46.
[22] Valiev RZ, Estrin Y, Horita Z, Langdon TG, Zehetbauer MJ, Zhu YT. Producing Bulk Ultrafine-Grained Materials by Severe Plastic Deformation. Jom 2006;68:33–9.
[23] Edalati K, Horita Z. A review on high-pressure torsion (HPT) from 1935 to 1988. Mater Sci Eng A 2016;652:325–52.
[24] N. R. Tao JL and KL. Surface nanocrystallization by surface mechanical attrition treatment. Mater Sci Forum 2008;579:91–108.
[25] Azadmanjiri J, Berndt CC, Kapoor A, Wen C. Development of surface nano-crystallization in alloys by surface mechanical attrition treatment (SMAT). Crit Rev Solid State Mater Sci 2015;40:164–81.
[26] Couillaud S, Enoki H, Amira S, Bobet JL, Akiba E, Huot J. Effect of ball milling and cold rolling on hydrogen storage properties of nanocrystalline $TiV_{1.6}$ $Mn_{0.4}$ alloy 2009;484:154–8.
[27] http://www.sonats-et.fr.
[28] Samih Y, Beausir B, Bolle B, Grosdidier T. In-depth quantitative analysis of the microstructures produced by Surface Mechanical Attrition Treatment (SMAT). Mater Charact 2013;83:129–38.
[29] Beausir B, Fundenberger J-J. Analysis Tools for Electron and X-Ray diffraction, ATEX - software, www.atex-software.eu, Université de Lorraine -Metz 2017.
[30] Liu Y, Jin B, Lu J. Mechanical properties and thermal stability of nanocrystallized pure aluminum produced by surface mechanical attrition treatment. Mater Sci Eng A 2015;636:446–51.
[31] Wang K, Tao NR, Liu G, Lu J, Lu K. Plastic strain-induced grain refinement at the nanometer scale in copper. Acta Mater 2006;54:5281–91.
[32] Blonde R, Chan HL, Allain-Bonasso N, Bolle B, Grosdidier T, Lu J. Evolution of texture and microstructure in pulsed electro-deposited Cu treated by surface mechanical attrition treatment (SMAT). J Alloys Compd 2010;504:S410–3.
[33] Zhang H., Hei Z., Liu G, Lu J, Lu K. Formation of nanostructured surface layer on AISI 304 stainless steel by means of surface mechanical attrition treatment. Acta Mater 2003;51:1871–81.
[34] Bagherifard S, Slawik S, Fernández-Pariente I, Pauly C, Mücklich F, Guagliano M. Nanoscale surface modification of AISI 316L stainless steel by severe shot peening. Mater Des 2016;102:68–77.
[35] Novelli M, Fundenberger J-J, Bocher P, Grosdidier T. On the effectiveness of surface severe plastic deformation by shot peening at cryogenic temperature. Appl Surf Sci 2016;389:1169–74.
[36] Novelli M, Bocher P, Grosdidier T. Effect of cryogenic temperatures and processing parameters on gradient-structure of a stainless steel treated by ultrasonic surface mechanical attrition treatment. Mater Charact 2018;139:197–207.
[37] Panda S, Toth LS, Fundenberger J, Perroud O, Guyon J, Zou J, et al. Analysis of heterogeneities in strain and microstructure in aluminum alloy and magnesium processed by high-pressure torsion. Mater Charact 2017;123:159–65.
[38] Wanagel J, Sass SL, Batterman BW. Observations on the microstructure and orientation relations in the vanadium-hydrogen system. Metall Trans 1974;5:105–9.
[39] Karpov VY, Rysina AM, Shapovalov VI, Mukhachev AP, Ostrin GY. Application of hydrogenation for the refining and pulverization of metals. Int J Hydrogen Energy 1996;21.
[40] Okumura M, Ikado A, Saito Y, Aoki H. Pulverization mechanism of hydrogen storage alloys on microscale packing structure. Int J Hydrogen Energy 2012;37:10715–23.
[41] Lu W, Ou S, Lin M, Wong M. Hydrogen absorption / desorption performance of Mg-

Al alloys synthesized by reactive mechanical milling and hydrogen pulverization. J Alloys Compd 2016;682:318–25.
[42] Hohenwarter A, Wurster S. Deformation and fracture characteristics of ultra fine-grained vanadium. Mater Sci Eng A 2016;650:492–6.
[43] Torres P, Aoyagi K, Suda T, Watanabe S, Ohnuki S. Hydride formation and fracture of vanadium alloys. J Nucl Mater 2002;307–311:625–9.
[44] Edalati K, Uehiro R, Fujiwara K, Ikeda Y, Li H, Sauvage X, et al. Ultra-severe plastic deformation : evolution of microstructure , phase transformation and hardness in immiscible magnesium-based systems. Mater Sci Eng A 2017;701:158–66.
[45] Subrata P, Toth LS, Zou J, Grosdidier T. Effect of strain heterogeneities on microstructure, texture, hardness, and H-activation of high-pressure torsion Mg consolidated from different powders. Materials 2018;11:1335–44.